

# Study of interaction of high-power $\text{Ar}^+$ laser beam with $\text{Ag}^+$ -doped glass

A. Nahal<sup>†</sup>, H. R. M. Khalesifard<sup>†</sup>, and M. Payami<sup>†,‡</sup>

March 31, 2022

<sup>†</sup>-*Department of Physics, Institute for Advanced Studies in Basic Sciences (IASBS),  
P.O.Box 45195-159, Zanjan-Iran*

<sup>‡</sup>-*Center for Theoretical Physics and Mathematics, Atomic Energy Organization of Iran,  
P. O. Box 11365-8486, Tehran, Iran*

## Abstract

In this work, we have investigated the interaction of a high-power  $\text{Ar}^+$  laser beam, in a continuous multi-line regime, with  $\text{Ag}^+$ -doped glass samples. The samples were subjected to the irradiation after the ion-exchange step. As a result of the irradiation, a peak appears in the absorption spectrum; its evolution depends on both the exposure time and the laser beam power. Interaction of the beam with the clusters causes them break into smaller ones which has been confirmed by optical absorption spectroscopy. Depending on the increment steps of the laser-beam power, different results are obtained. It is found that, in addition to the fragmentations of the nano-clusters, clusters of micro-meter size ( $d \sim 3\mu\text{m}$ ) are formed in the sample, if the laser power is increased in a fast regime. The fragmentation processes have been explained in the framework of the density-functional theory with stabilized jellium model.

# 1 Introduction

Nonlinear optical materials, such as glasses doped with metallic clusters, are promising ones for optical switching technology [1]. These materials, because of their high transparency; ease of fabrication; durability and thermomechanical stability, are essential component parts of functional devices for optical communications, sensing and computing[2, 3, 4]. Metal nano-cluster composites are particularly interesting because, depending on the choice of the metal and the dielectric host, they exhibit different pico-second relaxation times, range of chemical reactivities, and photo-sensitivities[5]

Several methods have been reported on producing and manipulating of metal-cluster doped-glasses: Low-mass ion irradiation[6, 7, 8, 9], annealing in hydrogen atmosphere after the ion-exchange (IE) process[10], and induced modifications of nano-clusters by pulsed laser beam[5].

In this paper, we report the results of interaction of a CW high-power  $\text{Ar}^+$  laser beam with  $\text{Ag}^+$ -doped glass samples, in two regimes of “slow” (SR) and “fast” (FR). In the SR, the power of the pump beam has been increased from 0.1 *mW* to 8 *W* in a period of  $\sim 90$  minutes ( 0.5 *W* increment per 5 minutes ). In the FR, the power is increased up to 8 *W* in 1 minute. The irradiation of the samples has been performed after the IE step.

The outcome of the SR results show that a 410 nm peak is appeared in the absorption spectrum and the peak in the UV region of the spectrum has been blue-shifted relative to that of non-irradiated samples. The appearance of the 410 nm band peak implies the generation of neutral Ag clusters[11], and the blue-shift of the peak in the UV region implies the generation of smaller clusters[12]. Both these features can be explained on the basis of possible fragmentation processes of the ionized nano-clusters. The evolution of these peaks are found to depend on the exposure ( $H = I.t$ , where  $I$  is the intensity and  $t$  is the exposure time).

In the FR, also the 410 nm peak is appeared but, in this case, the UV peak is blue-shifted relative to that in the SR results. In addition, in the FR, we have observed the generation of micro-clusters. These experimental facts are discussed in detail in the next section.

The organization of this paper is as follows. In section 2 we explain the details of the experiments and discuss the results. Section 3 is devoted to the density-functional calculations of the possible fragmentations of singly-ionized and doubly-ionized silver clusters, and finally, we conclude our work in section 4.

## 2 Experiments and discussions

In our experiments, the samples are prepared using the well-known ion-exchange (IE) method. In the IE process, some of the  $\text{Ag}^+$  ions in the molten salt and the  $\text{Na}^+$  ions in the glass matrix are exchanged by diffusion through the interfaces at both sides[13]. The diffusion depth and the concentration of the  $\text{Ag}^+$  ions in the glass matrix depend on the temperature of the molten salt, the IE duration, and the  $\text{Ag}^+$  concentration in the molten salt. In this experiment, we insert a glass slide ( $20 \times 30 \times 1.8$  mm) into the molten  $\text{NaNO}_3/\text{AgNO}_3$  mixed-salt (98%/2%) of temperature  $320^\circ\text{C}$  for 4 hours (Fig. 1). The glass components of our samples are specified in Table 1. The setup used to study the interaction of  $\text{Ar}^+$  laser (pump beam) with the prepared samples is sketched in Fig. 2. In this setup, the samples are subjected to the pump beam at the angle of incidence close to the normal. We have performed the experiments in two regimes of irradiation: The SR and the FR. Depending on which regime is chosen, different outcomes result in.

One of the common features observed in both regimes, during the irradiation process, is the formation of a micro-lens at the incidence point due to thermal effects induced by the pump beam. Formation of the micro-lens is implied by the appearance of a circular interference pattern on the screen (Fig. 2 top left). This pattern is generated due to interference of the reflected beams from the front and back sides of the sample, which have obtained different radii of curvatures (In the SR, the formation of this micro-lens is initiated beyond a threshold of  $P_t \sim 4$  W). For a fixed intensity of the pump beam, the radii of these pattern rings increase with the exposure time up to a limiting value for which a local thermal equilibrium has been achieved. The other common feature, observed in both regimes, is the appearance of a 410 nm band peak and weakening of the peak at the UV region of the absorption spectra (Fig.3). In this work, all spectra have been measured using a *Varian Cary-5* UV-Vis-NIR spectrophotometer. The dimension-less quantity  $D$  in the absorption spectra refers to the optical density

$$D = -\log\left(\frac{I}{I_0}\right), \quad (1)$$

where,  $I$  is the intensity of the probe beam and  $I_0$  is the intensity of the reference beam in the spectrophotometer. The 410 nm peak is resulted from the excitation of the surface plasmons of neutral silver clusters[11]. The neutral silver clusters can be created through different possible processes. In a fragmentation process, an ionized cluster may decay to smaller parts, one of which could be a neutral cluster. These fragmentation processes are discussed in detail in section 3. Another process could be the capture of the electron, detached from another cluster.

However, there are remarkable differences in the spectra of the two regimes: In the

FR (curve 1 of Fig. 4), the 410 nm peak is narrower and higher than that of the SR (curve 2 of Fig.4). In addition, a blue-shift is modulated on the UV peak of the FR spectra compared to that of the SR. The blue-shift in the spectra of the FR implies the production of smaller clusters due to fragmentation[12] The difference in the shapes of the 410 nm peaks in the two regimes originates from the different size distributions of the clusters in the irradiated samples. In general, a sharper peak implies a sharper size distribution of clusters.

## 2.1 Results under the Slow Regime

Under the SR condition, we notice the creation of neutral Ag clusters, which is implied by the appearance of a 410 nm band peak in the absorption spectra (Curve 2, Fig. 4).

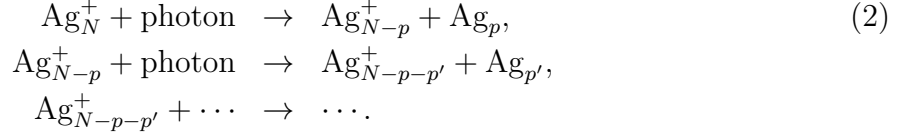
To analyze the spectra from different parts of the interaction region, we have divided the circular-shape interaction region into smaller sub-regions, along the diameter, separated by 0.2 mm and have measured their respective spectra. The results are shown in Fig. 5. Labels 1, 2, ..., 12 in Fig. 5 correspond to the sub-regions from the outer parts towards the center of the interaction region, respectively. As is seen, with moving towards the center, the height of the 410 nm peak increases and at the same time, the height of the UV-region peak decreases. This decrease is accompanied by a blue-shift. These behaviors are explained as follows. It is well-known that the intensity profile across the laser beam is Gaussian, i.e., the central part of the interaction region receives more photons than the outer parts. Knowing this fact, and considering the curves 1, 2, ..., 12 of Fig. 5 one can argue that, the more photons received by the sample glass, the more fragmentations of the clusters are induced. As a result of these fragmentations, the neutral Ag clusters are produced. We will show in section 3 that for large ionized clusters the fragmentations in which one of the products is neutral, are most favored (evaporation processes).

In Fig. 6, we have plotted the height of the 410 nm absorption peak as a function of the radial distance in the interaction region. The heights are normalized to the maximum height at the center. The center of the interaction region is located at point 2.4 mm (The size of the interaction region is taken to be 4.8 mm). This plot re-confirms the Gaussian intensity distribution.

The relative blue-shifts of the peaks at the UV region of the absorption spectra in different sub-regions (Fig. 5), imply that the sizes of the clusters decrease[12] as we move towards the central sub-region (the UV peak corresponds to the volume plasmon excitations of Ag clusters [See Ref. 11, page 35]). At the same time, one sees that the height of the UV peak decreases by moving towards the central sub-region. This weakening is due to the decrease in the concentration of clusters as a result of interaction with the pump beam. In fact, the pump beam causes the clusters fragment and scatter

in such a way that the conservation of momentum is satisfied.

Some of the mechanisms underlying the production of the neutral clusters, responsible for the 410 nm peak, could be the following chain fragmentation:



The fragmentation of large multiply ionized clusters (if any) are less favored because, they require photons with higher energies. The theoretical calculations related to the fragmentations of silver clusters has been discussed in section 3.

Another mechanism for production of the neutral clusters is recombination of the singly ionized clusters with the electrons detached from other possible neighboring sources (glass matrix):



Heating the non-irradiated ion-exchanged samples, under the normal atmosphere conditions for temperature beyond the ion-exchange temperature, leads to the appearance of 410 nm peak in the absorption spectra and a red-shift in the UV peak of the absorption spectra (Fig. 7). This experimental observation justifies the mechanism of Eq. (3).

## 2.2 Results under the fast regime

Under the FR condition, as under the SR, the creation of the 410 nm peak is observed. Comparing the absorption spectra of the central parts of the interaction regions in the two regimes, reveal that in the FR, this peak is narrower and higher; and in addition, the UV peak is blue-shifted as well as decreased relative to that in the SR results (Curve 1, Fig. 4). As mentioned before, a sharper peak corresponds to a sharper size distribution of clusters, and the blue-shift of the UV peak is related to the production of smaller clusters. To understand the detailed mechanisms responsible for these differences between the SR and the FR, more experimental investigations are needed.

In addition to the above-mentioned differences, under the FR, we have observed the generation of micrometer clusters. This experimental fact is discussed as follows.

After the irradiation under the FR, the appearance of large ( $\sim \mu\text{m}$ ) neutral Ag clusters has been observed at both sides of the sample. The distributions of the  $\mu\text{m}$ -clusters at the two sides have significant differences. The observations have been done by an optical microscope using bright-field photography method.

On the front side, the neutral  $\mu\text{m}$ -clusters are resided in a ring-shape area as islands. Each of these islands is formed, at a nucleation center, by absorbing its surrounding nano-clusters [Fig. 8(a)-(c)]. The nucleation centers mostly lie in relatively cold regions in the glass matrix which corresponds to the lower-intensity parts of the incidence area (the laser beam has a gaussian profile of intensity). However, because of the inhomogeneity of the glass matrix, some parts in the inner region have also higher viscosities[1, 14] which serve as nucleation centers. Due to the radial gradient in the laser-beam intensity, the radiation pressure varies in the radial direction which, in turn, cause the relatively larger clusters ( $d \gg \lambda/20$ ) in the central-part be pushed away from the center[15, 16, 17]. The radial velocities of the clusters decrease with distance from the center. Thus, they can aggregate mostly in the ring-shape region. On the back side of the sample, on the other hand, the  $\mu\text{m}$ -clusters are seen to be distributed more or less uniformly in a disc-shape area, centered at the beam center [Fig. 8(d), (e)]. This difference in the distributions at the front and back sides can easily be explained by comparing the beam intensities at these two sides. On measuring the transmittance of the beam for each line of the laser beam, we conclude that during the irradiation, the intensity at the back side is much less than the front side (Table 2), so that the mobility of the clusters is much less than that of the front side. This cause the back-side clusters not to be pushed away from the center but, just aggregate at those nucleation centers which correspond to the more viscous parts of the glass matrix[18]. To our knowledge, the formation of the  $\mu\text{m}$ -sized silver clusters in the glass matrix under the action of a CW laser beam has not been reported.

### 3 Theoretical study of the fragmentation processes

In the context of stabilized jellium model (SJM)[19] and self-consistent solution of the Kohn-Sham (KS) equations[20] in the density functional theory[21] with local spin-density approximation, we have calculated the total energies[22] of Ag clusters and thereby obtained the energies needed for the fragmentation via different decay channels. In the SJM, the discrete ions are replaced by a uniform positive charge background of density  $n = 3/4\pi r_s^3$  in which  $r_s$  is the bulk value of the Wigner-Seitz (WS) radius of the valence electrons of the metal and for Ag,  $r_s = 3.02 \text{ bohrs}$ . The geometry chosen for the positive background is spherical. We have studied the binary decay processes of positively charged  $\text{Ag}_N^+$ ,  $\text{Ag}_N^{2+}$  clusters containing up to  $N = 100$  atoms in all possible channels. We have considered the following possible decay processes for singly ionized Ag clusters

$$\text{Ag}_N^{1+} \rightarrow \text{Ag}_{N-p}^{1+} + \text{Ag}_p^0, \quad p = 1, 2, \dots, N-1. \quad (4)$$

For doubly charged clusters, the decays can proceed via two different processes. The first one is the evaporation process

$$\text{Ag}_N^{2+} \rightarrow \text{Ag}_{N-p}^{2+} + \text{Ag}_p^0, \quad p = 1, 2, \dots, N-3 \quad (5)$$

and the second one is fission into two charged products

$$\text{Ag}_N^{2+} \rightarrow \text{Ag}_{N-p}^{1+} + \text{Ag}_p^{1+}, \quad p = 1, 2, \dots, [N/2]. \quad (6)$$

In evaporation processes, the negativity of the difference between total energies before and after fragmentation (dissociation energy),

$$D^Z(N, p) = (E_{N-p}^Z + E_p^0) - E_N^Z, \quad (7)$$

is sufficient to have a spontaneous decay. However, in fission processes, because of the possible existence of a fission barrier, the negativity of the dissociation energy is not a sufficient condition for the fission of the parent cluster. In Fig. 9, the fission of a  $Z$ -ply charged  $N$ -atom cluster into two clusters of respective sizes  $N_1$ ,  $N_2 = N - N_1$ , and respective charges  $z_1$ ,  $z_2 = Z - z_1$  is schematically shown. For the fission, we have used the two-spheres approximation.  $Q_f$  is the energy release,  $B_c$  is the fusion barrier which is equal to the maximum energy of the Coulomb interaction of two positively-charged conducting spheres, taking their polarizabilities into account.  $B_f$  is the fission barrier height which is defined as

$$B_f = -Q_f + B_c. \quad (8)$$

The Coulomb interaction energy of two charged metal spheres has been numerically calculated using the classical method of image charges[23]. The calculations show that the maximum of the interaction energy is achieved for separations  $d_0 \geq R_1 + R_2$ . The most favored channel for the evaporation is defined as the channel for which the dissociation energy is minimum. Similarly, the most favored channel for the fission has the minimum of the barrier height.

### 3.1 Calculation of the total energy of a cluster

In the context of the SJM, the total energy of an  $N$ -atom  $Z$ -ply charged cluster is given by

$$\begin{aligned} E_{\text{SJM}}[n_{\uparrow}, n_{\downarrow}, n_{+}] &= E_{\text{JM}}[n_{\uparrow}, n_{\downarrow}, n_{+}] + \left( \varepsilon_M(r_s^B) + \bar{w}_R(r_s^B, r_c^B) \right) \int d\mathbf{r} n_{+}(\mathbf{r}) \\ &\quad + \langle \delta v \rangle_{\text{WS}}(r_s^B, r_c^B) \int d\mathbf{r} \Theta(\mathbf{r}) [n(\mathbf{r}) - n_{+}(\mathbf{r})], \end{aligned} \quad (9)$$

where

$$E_{\text{JM}}[n_{\uparrow}, n_{\downarrow}, n_{+}] = T_s[n_{\uparrow}, n_{\downarrow}] + E_{xc}[n_{\uparrow}, n_{\downarrow}] + \frac{1}{2} \int d\mathbf{r} \phi([n, n_{+}]; \mathbf{r}) [n(\mathbf{r}) - n_{+}(\mathbf{r})] \quad (10)$$

and

$$\phi([n, n_{+}]; \mathbf{r}) = \int d\mathbf{r}' \frac{[n(\mathbf{r}') - n_{+}(\mathbf{r}')]}{|\mathbf{r} - \mathbf{r}'|}. \quad (11)$$

Here,  $n = n_{\uparrow} + n_{\downarrow}$  which satisfies  $\int d\mathbf{r} n(\mathbf{r}) = N - Z$ , and  $n_{+}$  is the jellium density which satisfies  $\int d\mathbf{r} n_{+}(\mathbf{r}) = N$ .  $\Theta(\mathbf{r})$  takes the value of unity inside the jellium background and zero, outside. The first and second terms in the right hand side of Eq.(10) are the non-interacting kinetic energy and the exchange-correlation energy, and the last term is the Coulomb interaction energy of the system. The quantity  $\langle \delta v \rangle_{\text{WS}}$  is the average of the difference potential over the Wigner-Seitz cell and the difference potential,  $\delta v$ , is defined as the difference between the pseudo-potential of a lattice of ions and the electrostatic potential of the jellium positive background. All equations throughout this paper are expressed in atomic units ( $\hbar = e^2 = m = 1$ ), otherwise, they will be explicitly specified. Using the Eq. (21) of Ref. [19], this average value is given by

$$\langle \delta v \rangle_{\text{WS}}(r_s^B, r_c^B) = \frac{3(r_c^B)^2}{2(r_s^B)^3} - \frac{3}{10r_s^B}, \quad (12)$$

where,  $r_c^B$  is the core radius of the pseudo-potential and is given by[22]

$$r_c^B = \frac{1}{3}(r_s^B)^{3/2} \left\{ \left[ -2t_s(r_s) - \varepsilon_x(r_s) + r_s \frac{\partial}{\partial r_s} \varepsilon_c(r_s) - \varepsilon_M(r_s) \right]_{r_s=r_s^B} \right\}^{1/2}. \quad (13)$$

The quantities  $t_s$ ,  $\varepsilon_x$ , and  $\varepsilon_c$  are the kinetic, exchange, and correlation energies per electron, respectively[24]. The effective potential, used in the self-consistent KS equations, is obtained by taking the variational derivative of the SJM energy functional with respect to the spin densities as

$$v_{eff}^{\sigma}([n_{\uparrow}, n_{\downarrow}, n_{+}]; \mathbf{r}) = \phi([n, n_{+}]; \mathbf{r}) + v_{xc}^{\sigma}([n_{\uparrow}, n_{\downarrow}]; \mathbf{r}) + \Theta(\mathbf{r}) \langle \delta v \rangle_{\text{WS}}(r_s^B, r_c^B), \quad (14)$$

where  $\sigma = \uparrow, \downarrow$ . By solving the KS equations

$$\left( -\frac{1}{2} \nabla^2 + v_{eff}^{\sigma}(\mathbf{r}) \right) \psi_i^{\sigma}(\mathbf{r}) = \varepsilon_i^{\sigma} \psi_i^{\sigma}(\mathbf{r}), \quad \sigma = \uparrow, \downarrow, \quad (15)$$



and finding the self-consistent values for  $\varepsilon_i^\sigma$  and  $\psi_i^\sigma$ , with

$$n(\mathbf{r}) = \sum_{i(occ), \sigma=\uparrow, \downarrow} |\psi_i^\sigma(\mathbf{r})|^2, \quad (16)$$

the total energy of a cluster is calculated.

## 3.2 Results of Calculations

After the self-consistent calculations, we have calculated the total energies of  $\text{Ag}_N^Z$  ( $Z=0,1,2$ ) for different cluster sizes ( $1 \leq N \leq 100$ ). Then, using Eqs. (7) and (8), we have calculated the dissociation energies and the fission barriers.

In Fig. 10, we have plotted the dissociation energies of the most favored evaporation channels of the singly ionized clusters. We have shown the most favored value of  $p$  by  $p^*$ . The solid small square symbols show the most favored values  $p^*$  on the right vertical axis whereas, the corresponding dissociation energies,  $D^{1+}(N, p^*)$ , are shown on the left vertical axis by large open squares. As is seen in the figure, there exist some maxima and minima. The maxima of the  $D^Z(N, p^*)$  correspond to the closed-shell  $\text{Ag}_N^+$  clusters with  $N=3, 9, 19, 35, 59, \dots$ . These clusters have high stabilities compared to their neighboring sizes. On the other hand, the minima correspond to the sizes which decay into two closed-shell clusters (for example,  $\text{Ag}_{11}^+ \rightarrow \text{Ag}_9^+ + \text{Ag}_2$ ). A negative value for the dissociation energy implies that the cluster is unstable against the spontaneous decay.

In Fig. 11(a), we have shown the most favored products  $\text{Ag}_{p^*}^0$  and the dissociation energies  $D^{2+}(N, p^*)$  for the decay of  $\text{Ag}_N^{2+}$  via evaporation channel. It is seen that the most favored products are mainly monomers, dimers and octamers. On the other hand, here, the mean dissociation energy is higher than that in the evaporation of singly ionized clusters. That is, here, the number of clusters stable against the spontaneous evaporation is larger than that in the singly ionized case. Evaporation is not the only decay mechanism for multiply charged clusters, and they can also decay via fission processes in which both fragments are charged.

Figure 11(b) shows the barrier heights  $B_f(N, p^*)$  for the most favored fission channels  $\text{Ag}_N^{2+} \rightarrow \text{Ag}_{N-p^*}^+ + \text{Ag}_{p^*}^+$ . By definition, the most favored fission channel has a minimum value for the barrier height. As is seen, for small clusters, the majority have negative barrier heights. That is, most of them are unstable against spontaneous fission. However, as  $N$  increases, the number of clusters with negative barrier heights decreases and beyond a certain size range, all the barrier heights become positive.

A doubly charged cluster decays both via evaporation and fission. At small sizes ( $N < 21$ ), the fission process dominates because, the barrier heights for the fission are

lower than the dissociation energies for the evaporation. This situation is shown in Fig. 11(c). As is seen, the competition between the evaporation and fission starts at  $N=21$ . This competition continues with some fluctuations until the evaporation dominates completely. Since, the cluster sizes in the a ion-exchanged sample are[5] of order  $\sim 5$  nm, which corresponds to  $N \gg 21$ , the fragmentations mostly proceed via the evaporation mechanism.

## 4 Conclusion

We have studied the interaction of a CW laser beam with the clusters embedded in glass matrix. The study consists of two regimes of fast and slow. In both regimes, neutral clusters are generated (creation of a 410 nm band peak). Depending on the regime, different results are obtained. In the slow regime, the absorption peak in the UV region of the spectrum is blue-shifted relative to that of non-irradiated samples, which implies the generation of smaller clusters. On the other hand, under the fast regime, in addition to the fragmentations, clusters of  $\mu\text{m}$  size are created. The experimental results show that heat treatment of the ion-exchanged sample under the normal atmosphere conditions also gives rise to the appearance of neutral clusters. The theoretical calculations show that doubly ionized clusters of size  $N \gg 21$  decay mostly via the evaporation mechanism which is one of the possible mechanism for the generation of neutral clusters.

## Acknowledgement

The authors are grateful to M. T. Tavassoli for his advice in some experiments. They also appreciate A. Ghoreyshi for determination of components of glass samples. The financial support of this work is provided by research council of the Institute for Advanced Studies in Basic Sciences.

## References

- [1] E. M. Vogel, J. Am. Ceram. Soc. **72**, 719 (1989).
- [2] T. Kobayashi, Nonlinear Optics **1**, 91 (1991).
- [3] S. R. Friberg and P. W. Smith, IEEE J. Quantum Electron. **QE-23**, 2089 (1987).
- [4] G. I. Stegeman and R. H. Stolen, J. Opt. Soc. Am. B **6**, 652 (1989).
- [5] F. Gonella *et. al.*, Appl. Phys. Lett. **69**, 3101 (1996).
- [6] F. Caccavale *et. al.*, Nucl. Instrum. Meth. B **96**, 382 (1995).
- [7] G. Battaglin *et. al.*, J. Non-Cryst. Solids **196**, 79 (1996).
- [8] G. Battaglin *et. al.*, Proc. SPIE **3405**, 533 (1997).
- [9] F. Gonella *et. al.*, Nucl. Instrum. Meth. B **127/128**, 562 (1996).
- [10] G. De Marchi *et. al.*, Appl. Phys. A **61**, 403 (1996).
- [11] U. Kreibig and M. Vollmer, *Optical Properties of Metal Clusters*, (Springer 1995).
- [12] V. V. Kresin, Phys. Rev B **51**, 1844 (1995).
- [13] S. I. Najafi, *Introduction to Glass Integrated Optics*, (Artech House, 1992).
- [14] O. V. Mazurin and E. A. Porai-Koshits, Eds., *Phase Separation in Glass* (North-Holland 1984).
- [15] S. Sasaki *et. al.*, Appl. Phys. Lett. **60**, 807 (1992).
- [16] K. Svoboda and S. M. Block, Opt. Lett. **19**, 930 (1994).
- [17] P. Zemánek, A. Jonáš, L. Ššámek, and M. Liška, Opt. Commun. **151**, 273 (1998).
- [18] W. Vogel, *Chemistry of Glass*, (The American Ceramic Society 1985) p. 153.
- [19] J. P. Perdew, H. Q. Tran, and E. D. Smith, Phys. Rev. B **42**, 11627 (1990).
- [20] W. Kohn and L. J. Sham, Phys. Rev. **140**, A1133 (1965).
- [21] P. Hohenberg and W. Kohn, Phys. Rev. B **136**, 864 (1964).

- [22] M. Payami, J. Phys.: Condens. Matter **13**, 4129 (2001).
- [23] U. Näher, S. Bjørnholm, S. Frauendorf, F. Garcias, and C. Guet, Phys. Rep. **285**, 245 (1997) and references therein.
- [24] M. Payami and N. Nafari, J. Chem. Phys. **109**, 5730 (1998).

Figure 1: Schematic drawing of the ion-exchange process in sample preparation. As a diffusion process, the  $\text{Ag}^+$  ions in the molten salt replace the  $\text{Na}^+$  ions in the glass matrix.

Figure 2: Experimental setup for irradiating the samples. The circular interference pattern, shown on the top-left, is appeared beyond the threshold power ( $P_t \sim 4 \text{ W}$ )

Figure 3: Absorption spectra of the samples 1)- before, 2)- after the irradiation by the high-power  $\text{Ar}^+$  laser beam. The quantity  $D$  in the vertical axis corresponds to the dimension-less optical density. The 410 nm absorption band peak is appeared after the irradiation.

Figure 4: Comparison of the absorption spectra under the fast regime (curve 1) and the slow regime (curve 2). The spectra are measured for the central parts of the interaction regions.

Figure 5: Absorption spectra from different parts of the interaction region. The labels 1-12 correspond to the sub-regions from the outer parts to the center of the circular interaction region, respectively. The sub-regions are separated by  $0.2 \text{ mm}$ .

Figure 6: Plot of the normalized height of the 410 nm absorption band peak as a function of the radial distance in the circular interaction region.

Figure 7: Absorption spectra of a sample. 1)- before and 2)- after heat treatment at  $350^\circ\text{C}$  for 2 hours. After the heat treatment, a weak 410 nm absorption peak is appeared and the UV peak is red-shifted as well as increased

Figure 8: Micro-graphs of the interaction area of the sample after irradiation under the fast regime. a)- The ring-shape area on the front side of the sample with an island-like texture (50X). b)- Area A in (a) is magnified (700X). c)- The rectangular region in (b) is magnified (2000X). d)- Magnification of the area B in (a) which belongs to the back side of the sample (300X), indicating the formation of a dot-like texture. This photo is taken by the dark-field method. e)- Magnified (700X) rectangular region of photo (d).

Figure 9: Fission barrier in the two-spheres approximation. The parent  $N$ -atom  $Z$ -ply charged cluster decays into clusters of sizes  $N_1$  and  $N - N_1$ , with charges  $Z_1$  and  $Z_2$ , respectively.

Figure 10: Dissociation energies, in electron volts, of the most favored decay channels of singly ionized clusters are shown with respect to the left vertical axis. The right vertical axis shows the sizes of the fragments in the most favored channels.

Figure 11: a)- The same quantities as in Fig.10 for doubly ionized clusters, b)- the fission barrier height in electron-volts for the most favored fission channel as a function of the cluster size. The right vertical axis shows the most favored product sizes of the neutral clusters, c)- comparison of the decay energies of via evaporation and fission mechanisms. Competition starts at  $N = 21$

Component	SiO <sub>2</sub>	CaO	Na <sub>2</sub> O	MgO	Al <sub>2</sub> O <sub>3</sub>	K <sub>2</sub> O	S	Fe <sub>2</sub> O <sub>3</sub>	P <sub>2</sub> O <sub>5</sub>
Weight Percent(%)	80	9.41	4	3.3	2.2	0.41	0.2	0.11	0.11

Table 1: Components of the glass, in weight percent, which was used in our experiments to produce the ion-exchanged samples.

Wavelength(nm)	457.9	476.5	488	496.5	514.5
Transmittance (%)	6.6	10.3	13.8	16.7	26.1

Table 2: Transmittance, in percent, of the ion-exchanged samples for different lines in the pump beam.

This figure "FIG1.JPG" is available in "JPG" format from:

<http://arxiv.org/ps/physics/0302073v1>

This figure "FIG2.JPG" is available in "JPG" format from:

<http://arxiv.org/ps/physics/0302073v1>



This figure "FIG3.JPG" is available in "JPG" format from:

<http://arxiv.org/ps/physics/0302073v1>

This figure "FIG4.JPG" is available in "JPG" format from:

<http://arxiv.org/ps/physics/0302073v1>

This figure "FIG5.JPG" is available in "JPG" format from:

<http://arxiv.org/ps/physics/0302073v1>

This figure "FIG6.JPG" is available in "JPG" format from:

<http://arxiv.org/ps/physics/0302073v1>

This figure "FIG7.JPG" is available in "JPG" format from:

<http://arxiv.org/ps/physics/0302073v1>

This figure "FIG8.JPG" is available in "JPG" format from:

<http://arxiv.org/ps/physics/0302073v1>

This figure "FIG9.JPG" is available in "JPG" format from:

<http://arxiv.org/ps/physics/0302073v1>

This figure "FIG10.JPG" is available in "JPG" format from:

<http://arxiv.org/ps/physics/0302073v1>



This figure "FIG11A.JPG" is available in "JPG" format from:

<http://arxiv.org/ps/physics/0302073v1>

This figure "FIG11B.JPG" is available in "JPG" format from:

<http://arxiv.org/ps/physics/0302073v1>

This figure "FIG11C.JPG" is available in "JPG" format from:

<http://arxiv.org/ps/physics/0302073v1>